Solid State Sciences 107 (2020) 106294

Contents lists available at ScienceDirect

Solid State Sciences

journal homepage: http://www.elsevier.com/locate/ssscie

Transformation of trigonal planar B_4 into zigzag B_4 units within the new boride series $Ti_{2-x}M_{1+x-\delta}Ir_{3+\delta}B_3$ (x = 0.5 for M = V–Mn, x = 0 for M = Mn–Ni and $\delta < 0.2$)

Jan P. Scheifers [a,1], Michael Küpers [b,1], Yuemei Zhang [c], Laura Lutz–Kappelman [d], Gordon J. Miller [d], Boniface P.T. Fokwa *,[a]

[a] Department of Chemistry, University of California, Riverside, Riverside, CA, 92521, USA
[b] Institute of Inorganic Chemistry, RWTH Aachen University, Aachen, D-52056, Germany
[c] Department of Chemistry, Warren Wilson College, Asheville, NC, 28815, USA
[d] Department of Chemistry, Iowa State University, Ames, IA, 50011, USA

ARTICLE INFO

Keywords:
Borides
Trigonal planar B_4
Trans zigzag B_4
Ladders
Chains of triangles

ABSTRACT

In metal–rich borides, numerous boron fragments B_n (n = 2, 3, 4, 5, 6) have been discovered, the B_4 units being the most versatile with four different shapes (bent, zigzag, trigonal planar and tetrahedral). We report on the new boride series $Ti_{2-x}M_{1+x-\delta}Ir_{3+\delta}B_3$ (x = 0.5 for M = V–Mn, x = 0 for M = Mn–Ni and $\delta < 0.2$), in which a structural change occurs by successive substitution of the *3d* transition metal M = V, Cr, Mn, Fe, Co and Ni. It is found that the change in structure from the $Ti_{1+x}Os_{2-x}RuB_2$–type structure ($P\bar{6}2m$, no. 189) to the $Ti_{1+x}Rh_{2-x+y}Ir_{3-y}B_3$–type (*Pbam*, no. 55) leads to a change of B_4 shape from trigonal planar B_4 (*M* = V–Mn) to zigzag B_4 fragment (*M* = Mn–Ni). Even though there is no group–subgroup relationship between the two structures, we present how the $Ti_{1+x}Os_{2-x}RuB_2$–type structure can easily be geometrically derived from the $Ti_{1+x}Rh_{2-x+y}Ir_{3-y}B_3$–type.

1. Introduction

Metal borides are known for some set of characteristic properties such as high melting points, superior hardness, and chemical inertness that originate from their extraordinary crystal chemistry, in which strong boron–boron and metal–boron bonds play a key role [1–10]. The crystal chemistry of metal–rich borides has been enriched in recent years by the discovery of complex phases in which different boron fragments such as B_2, B_3, B_4, B_5 and B_6 were found [11–15]. In some cases, these compounds exhibit highly exciting properties: Superconductivity was observed in NbRuB (containing B_2 dumbbells) [16], in TaRuB and NbOsB (both containing zigzag B_4 units) [17], while itinerant ferrimagnetism was reported for $TiCrIr_2B_2$ (trigonal planar B_4 units) [18], itinerant ferromagnetism in arc-melted $Nb_6Fe_{1-x}Ir_{6+x}B_8$ (B_6 rings) [19] which becomes an itinerant ferrimagnet when annealed at 1600 °C [20]. Most of these boron fragments can be derived from the honeycomb boron layer of the AlB_2–type structure [3]. Accordingly, the fragments arise from boron–centered trigonal metal prisms sharing a rectangular face, thus leading to short boron–boron distances (typically 1.7 to 1.8 Å). For fragments with more than three boron atoms, different configurations are possible such as for the B_4 (zigzag–B_4 in Mo_2IrB_2 [21] and $Ti_{1+x}Rh_{2-x+y}Ir_{3-y}B_3$ types [22], bent–B_4 in β–Cr_2IrB_2 [13] or trigonal planar B_4 unit in the hexagonal $Ti_{1+x}Os_{2-x}RuB_2$ ($P\bar{6}2m$, no. 189) [23]. Recently, weak spin frustration and ferrimagnetic ordering below 275 K was found in $TiCrIr_2B_2$ ($Ti_{1+x}Os_{2-x}RuB_2$-type) and attributed to the unique substructure of the magnetic element, namely a chain of equilateral Cr_3 triangles [18] which strongly interacts with trigonal planar B_4 units. The discovery of this phase was the result of our increased efforts of designing new phases by incorporation of magnetic *3d* elements into new boride structures. Naturally, after discovering $TiCrIr_2B_2$, the next target was to study the substitution of Cr by other *3d* transition metals and its impact on the crystal structure and possibly magnetic properties. In the present work we report on the new boride series $Ti_{2-x}M_{1+x-\delta}Ir_{3+\delta}B_3$ (x = 0.5 for M = V–Mn, x = 0 for Mn–Ni and $\delta < 0.2$) in which a structural change occurs by successive substitution of the *3d* transition metal M = V, Cr, Mn, Fe, Co and Ni. Finally, we explain how the $Ti_{1+x}Os_{2-x}RuB_2$–type (with trigonal planar B_4 fragment) and the $Ti_{1+x}Rh_{2-x+y}Ir_{3-y}B_3$–type (with zigzag B_4 fragment) structures can be

* Corresponding author.
E-mail address: bfokwa@ucr.edu (B.P.T. Fokwa).
[1] co-first authors.

https://doi.org/10.1016/j.solidstatesciences.2020.106294
Received 31 January 2020; Received in revised form 23 April 2020; Accepted 15 May 2020
Available online 6 July 2020

geometrically derived from each other.

2. Experimental procedures

The boride phases were synthesized by a high temperature reaction in an electric arc furnace directly from the elements (more details on the synthesis can be found in the SI). Overall, three sets of samples were prepared with the starting compositions 2Ti:M:3Ir:3B, 1.5Ti:1.5M:3Ir:3B and Ti:2M:3Ir:3B, where M = V, Cr, Mn, Fe, Co or Ni. These three sets were prepared in order to investigate if the Ti:M ratio affects the type of boride obtained. Powders of the respective elements are mixed thoroughly in the corresponding ratio and pressed into dense pellets. The pellets are then arc-melted several times in the arc furnace (20 V voltage and 20 A applied current) which is filled with Ar. Small gray beads with metallic luster were obtained. Their weight was compared to the initial weight to keep track of any material lost during the reaction, but the loss turned out to be negligible. All samples were stable in air even after a long exposure time.

The beads were crushed, and single crystals were isolated from the powders under an optical microscope. The samples were then finely ground in an agate mortar and used to collect powder X–ray diffraction (PXRD) data, utilizing Cu K_α radiation (λ = 1.54059 Å) of a Stadi P powder diffractometer (STOE & Cie GmbH, Darmstadt, Germany) equipped with a Ge monochromator and an Image–plate detector. Each measurement took 3 h and covered a 2Θ range from 10° to 90°. The powder diffraction data was refined by a full–matrix least–squares refinement (Rietveld) as implemented in the FULLROF Suite [24,25].

In case suitable single crystals were isolated, they were subsequently used to collect single–crystal X–ray diffraction (SCXRD) data, utilizing Mo–$K_{\alpha1}$ radiation (λ = 0.71073 Å) of a Smart APEX diffractometer by Bruker equipped with a CCD detector. The structure was solved by direct methods using the SHELXS package and a full–matrix least–squares refinement was performed using SHELXL [26,27]. Additionally, the presence of the metals in the single crystals were confirmed by energy dispersive X–ray spectroscopy (EDX) with a LEO 1450VP electron microscope from Carl ZEISS.

3. Results and discussion

3.1. Phase analysis

In the powder diffraction data of all V- and Cr-containing samples the $Ti_{1+x}Os_{2-x}RuB_2$–type phase was identified. However, these samples contained additional compounds, mainly the Cu_3Au–type $TiIr_3B_{1-y}$ phase [28] in all of them and the τ–boride $Cr_{7.9}Ir_{14.1}B_6$ [13] for the two Cr samples with higher Cr-content (Ti:M = 1 and ½). For the Mn-containing samples with low Mn–content (Ti:M = 2 and 1), a structure change was observed as the $Ti_{1+x}Rh_{2-x+y}Ir_{3-y}B_3$–type phase [22] was obtained as main product, while for higher Mn–content (Ti:M = ½) only a minority $Ti_{1+x}Os_{2-x}RuB_2$–type phase [23] is present, the main phase being the τ–boride ($(Fe_{0.54}Ir_{0.46})_{20}Fe_3B_6$-type) [29]. The $(Ti_{1-x}Fe_x)_3Ir_3B_3$ samples contain a $Ti_{1+x}Rh_{2-x+y}Ir_{3-y}B_3$–type boride phase together with a τ–boride ($(Fe_{0.54}Ir_{0.46})_{20}Fe_3B_6$-type) [29] for all Ti:M ratios, and a third phase ($TiIr_3B_{1-y}$) [28] is found only for Ti:M = 2. The $(Ti_{1-x}M_x)_3Ir_3B_3$ samples with *M* = Co and Ni contain a $Ti_{1+x}Rh_{2-x+y}Ir_{3-y}B_3$–type boride only for Ti:M = 2. In these samples, some unindexed peaks are present, thus the weight fractions given in Tables S1, S2 and S3 (supporting information, SI) are just relative values.

3.2. Single-crystal structure determination

In order to refine the proper compositions of the new phases, single-crystal refinements coupled with EDX analyses were carried out. Due to the irregular shapes of the single crystals studied by EDX only qualitative measurements were possible, except for the orthorhombic Mn-based phase which yielded the metal ratio 2.4(2):0.7(2):2.9(2) for Ti:Mn:Ir, which is in fair agreement with the results obtained from single-crystal diffraction below. The crystallographic and structure refinement data are given in Tables 1 and 2, while Table 3, S4, S5, S6 and S7 contain the refined atomic positions and displacement parameters and Table 4 contain selected bond lengths (for a representative of each structure

Table 1
Crystallographic and structure refinement data of $Ti_{1-x}V_xIr_2B_2$ and $TiMn_{0.92(2)}Ir_{2.08(2)}B_2$ (obtained from the starting composition Ti:2Mn:3Ir:3B).

Formula	$Ti_{1-x}V_xIr_2B_2$	$TiMn_{0.92(2)}Ir_{2.08(2)}B_2$
space group, Z	$P\bar{6}2m$ *(no. 189); 3*	$P\bar{6}2m$ *(no. 189); 3*
formula weight (g/mol)	504.86	519.38
F(000)	627	645
lattice parameters		
a (Å)	8.601(2)	8.610(2)
b (Å)	8.601(2)	8.610(2)
c (Å)	3.1870(6)	3.1880(6)
V (Å^3)	204.18(6)	204.65(6)
calc. density (g/cm^3)	12.318	12.634
abs. coefficient (mm^{-1})	103.253	107.599
θ–range (°)	$4.74 < \theta < 35.69$	$4.74 < \theta < 35.78$
hkl–range	$-4 \le h \le 14$	$-13 \le h \le 14$
	$-14 \le k \le 13$	$-14 \le k \le 11$
	$-4 \le l \le 5$	$-4 \le l \le 5$
no. of reflections, R_{int}	1809; 0.0881	2166; 0.1373
indep. reflections	382	385
no. parameters	17	20
R_1; wR_2 (all *I*)	0.0639; 0.1037	0.0585; 0.1480
GooF	1.110	1.114
diff. peak/hole (e·Å^{-3})	−3.583/4.406	−6.070/7.444

indep. reflections	1082	1019	1063	618
no. parameters	46	37	46	41
R_1; wR_2 (*I* > 2sigma (*I*))	0.0588; 0.0912	0.0518; 0.0952	0.0610; 0.1133	0.0462; 0.1004
R_1; wR_2 (all *I*)	0.1111; 0.1045	0.0772; 0.1064	0.1103; 0.1294	0.0684; 0.1099
GooF	1.067	1.090	1.064	1.042
diff. peak/hole (e·Å^{-3})	−5.427/ 7.830	−4.965/ 5.601	−5.896/ 5.794	−4.455/ 3.404

Table 2
Crystallographic and single-crystal structure data of $Ti_2M_{1-x}Ir_{3+x}B_3$ obtained from the starting composition 2Ti:*M*:3Ir:3B with *M* = Mn, Fe and Co.

Formula	$Ti_2Mn_{0.83}{}_{(1)}Ir_{3.17(1)}B_3$	$Ti_2Fe_{0.91}{}_{(1)}Ir_{3.09(1)}B_3$	$Ti_2Co_{0.88}{}_{(1)}Ir_{3.12(1)}B_3$	$Ti_2Ni_{0.88}{}_{(1)}Ir_{3.12(1)}B_3$
space group, Z		*Pbam (no. 55); 4*		
formula weight (g/mol)	783.10	772.27	779.09	778.89
F(000)	1295	1281	1291	1295
lattice parameters				
a (Å)	8.639(2)	8.618(1)	8.60(2)	8.598(2)
b (Å)	15.004(4)	14.975(7)	15.00(3)	14.970(4)
c (Å)	3.228(7)	3.221(1)	3.225(5)	3.238(7)
V (Å^3)	418.4(9)	415.7(2)	416.0(2)	416.8(2)
calc. density (g/cm^3)	12.432	12.340	12.439	12.413
abs. coefficient (mm^{-1})	106.281	104.932	106.143	106.429
θ–range (°)	$4.71 < \theta <$ 35.93	$5.46 < \theta <$ 35.38	$4.72 < \theta <$ 35.76	$4.72 < \theta <$ 28.52
hkl–range	$-12 \le h \le 14$	$-13 \le h \le 14$	$-11 \le h \le 14$	$-11 \le h \le 7$
	$-16 \le k \le 24$	$-8 \le k \le 24$	$-22 \le k \le 24$	$-19 \le k \le 20$
	$-4 \le l \le 5$	$-4 \le l \le 5$	$-4 \le l \le 5$	$-4 \le l \le 4$
no. of reflections, R_{int}	4318; 0.1311	3320; 0.0681	4238; 0.1119	2331; 0.0934
indep. reflections	1082	1019	1063	618
no. parameters	46	37	46	41
R_1; wR_2 (*I* > 2sigma(*I*))	0.0588; 0.0912	0.0518; 0.0952	0.0610; 0.1133	0.0462; 0.1004
R_1; wR_2 (all *I*)	0.1111; 0.1045	0.0772; 0.1064	0.1103; 0.1294	0.0684; 0.1099
GooF	1.067	1.090	1.064	1.042
diff. peak/hole (e·Å^{-3})	−5.427/7.830	−4.965/5.601	−5.896/5.794	−4.455/3.404

Table 3
Atomic coordinates, site occupation factors (SOF) and displacement parameters of $TiMn_{0.92(2)}Ir_{2.08(2)}B_2$ and $Ti_2Ni_{0.88(1)}Ir_{3.12(1)}B_3$. U_{13} and $U_{23} = 0$.

$TiMn_{0.92(2)}Ir_{2.08(2)}B_2$										
Atom	Site	*x*	*Y*	*z*	SOF	U_{eq}	U_{11}	U_{22}	U_{33}	U_{12}
Ir1	6k	0.4636(2)	0.2760(2)	0.5	1	0.0096(3)	0.0058(4)	0.0058(5)	0.0190(5)	0.0042(4)
Mn2/Ir2	3f	0.1786(7)	0.1786(7)	0	0.93(2)/0.07(2)	0.0010(2)	0.014 (2)	0.005(2)	0.009(2)	
Ti3	3f	0.4174(9)	0	0	1	0.005(1)	0.006(2)	0.003(2)	0.011(2)	0.003(2)
B1	1b	0	0	0.5	1	0.028(9)	–	–	–	–
B2	3g	0	0.258(9)	0.5	1	0.028(9)	–	–	–	–
B3	2c	0.6667	0.3333	0	1	0.028(9)	–	–	–	–
$Ti_2Ni_{0.88(1)}Ir_{3.12(1)}B_3$										
atom	Site	*x*	*y*	*z*	SOF	U_{eq}	U_{11}	U_{22}	U_{33}	U_{12}
Ir1	4 h	0.0197(2)	0.09511(9)	0.5	1	0.0117(3)	0.0024(5)	0.0092(7)	0.0236(8)	0.0007(4)
Ir2	4 h	0.7148(2)	0.14228(9)	0.5	1	0.0118(4)	0.0024(6)	0.0095(7)	0.0236(7)	−0.0009(4)
Ir3	4 h	0.9337(2)	0.26982(9)	0.5	1	0.0129(4)	0.0029(5)	0.0097(7)	0.0262(8)	−0.0006(4)
Ir4/Ni4	4g	0.4748(4)	0.0858(2)	0	0.11(2)/0.89(2)	0.010(2)	0.006(2)	0.015 (2)	0.009 (2)	0.003(2)
Ti5	4g	0.1819(6)	0.2069(4)	0	1	0.0050(8)	0.005(2)	0.007(3)	0.002(3)	−0.001(2)
Ti6	4g	0.1985(6)	0.9962(4)	0	1	0.0050(8)	0.005(2)	0.007(3)	0.002(3)	−0.001(2)
B7	4 h	0.290(4)	0.099(3)	0.5	1	0.010(4)	–	–	–	–
B8	4 h	0.605(4)	0.006(3)	0.5	1	0.010(4)	–	–	–	–
B9	4g	0.890(4)	0.165(3)	0	1	0.010(4)	–	–	–	–

Table 4
Interatomic distances (Å) of $TiMn_{0.92(2)}Ir_{2.08(2)}B_2$ and $Ti_2Ni_{0.88(1)}Ir_{3.12(1)}B_3$.

$TiMn_{0.92(2)}Ir_{2.08(2)}B_2$		
Atom 1	Atom 2	d(atom1 – atom2) (Å)
B1	B2	2.22(6)
	Mn2	2.21(1)
B2	Mn2	2.10(4)
	Ti3	2.53(4)
	Ir1	2.14(2)
B3	Ir1	2.23(1)
	Ti3	2.59(1)
Ir1	Ir1	2.70(1) – 2.80(1)
Mn2	Mn2	2.61(1) –3.19(1)
$Ti_2Ni_{0.88(1)}Ir_{3.12(1)}B_3$		
B7	B8	1.81(6)
B8	B8	1.81(4)
B7	Ir1–3	2.28(2) – 2.47(3)
	Ti5, Ti6 & Ir4/Ni4	2.32(3) – 2.33(3)
B8	Ir1–3	2.25(3)
	Ti5, Ti6 & Ir4/Ni4	2.23(2) – 2.34(2)
B9	Ir1–3	2.23(2) – 2.29(2)
	Ti5, Ti6 & Ir4/Ni4	2.53(4) – 2.62(4)
Ir1–3	Ir1–3	2.68(1) – 2.87(1)
Ir4/Ni4	Ir4/Ni4	2.61(1) – 3.22(1)

type).

$TiMIr_2B_2$ (M = V, Mn): The structure of $Ti_{1+x}Os_{2-x}RuB_2$ [23] was used as model for the refinement of single–crystal data of the V– and Mn–based compounds since the PXRD data indicated isotypism of both compounds with $Ti_{1+x}Os_{2-x}RuB_2$. From the $TiOs_2RuB_2$ model, Os was substituted by Ir and Ru by M (V, Mn) leading to $TiMIr_2B_2$ as the starting model. The refinements converged in both cases smoothly. Since Ti and V cannot be distinguished using XRD (both are 1 electron apart and have similar atomic radius) and because EDX analysis had confirmed the presence of the two elements in the single crystal analyzed, the Ti– and V–sites were refined with a fixed 50:50 (Ti:V) mixed occupancy, thus the composition of this phase should be viewed as $(Ti_{1-x}V_x)_2Ir_2B_2$. In the case of M = Mn, the large difference in atomic radius between Ti and Mn was enough to differentiate both elements (similar to the reported M = Cr) [18]. However, disorder on the Mn site with the heavier Ir (8%) was necessary to fully occupy the site, leading to the refined chemical formula $TiMn_{0.92(2)}Ir_{2.08(2)}B_2$. Occupational disorder between a first-row transition metal and a 4*d* or 5*d* metal is frequently observed in metal borides such as $Nb_6Fe_{1-x}Ir_{6+x}B_8$ or $(Fe_{0.54}Ir_{0.46})_{20}Fe_3B_6$ [19,29]. Furthermore, the B–B distance had to be restrained to 1.85 Å (average B–B distance in $Ti_2MnIr_3B_3$, see below) as the refined distance was very large (2.22 Å), exceeding all other distances (1.75–1.90 Å) found for all B_4 units in this and related structure types.

$Ti_2MIr_3B_3$ (*M* = Mn, Fe, Co, Ni): PXRD data established isotypism of these four compounds with $Ti_{1+x}Rh_{2-x+y}Ir_{3-y}B_3$–type structure. Suitable single crystals could be isolated in all cases, and the composition "$Ti_{1+x}(Rh_{1-x})$ $(Rh_{1+y})Ir_{3-y}B_3$" was used as the starting model but replacing (Rh_{1-x}) and (Rh_{1+y}) by Ti and *M*, respectively, leading to the ideal starting formula $Ti_2MIr_3B_3$. In all cases, the refinements converged smoothly. However, a mixed occupancy on the *M* site with the heavier Ir was necessary to fully occupy the *M* site, leading to the general chemical formula $Ti_2M_{1-y}Ir_{3+y}B_2$ (y < 0.2). The B–B bond lengths range from 1.81 (5) Å to 1.90(5) Å for the outer B7–B8 bond and from 1.76(6) Å to 1.84 (6) Å for the central B8–B8 bond of the zigzag B_4 fragment. A list of the bond lengths for all compounds can be found in Tables S8 and S9 in the SI. In general, they fall into the expected range for intermetallic borides. The M–B and Ir–B bonds are roughly between 2.2 Å and 2.3 Å, while the Ti–B distances are mostly 2.4 Å or longer.

3.3. Structural descriptions

$(Ti_{1-x}V_x)_2Ir_2B_2$ and $TiMn_{0.92(2)}Ir_{2.08(2)}B_2$: All atoms are distributed in two layers at *z* = 0 and *z* = 0.5 along the *c* direction. All Ir atoms are found in the layer at *z* = 0.5 together with two out of three boron atoms (Fig. 1). The two boron atoms (B1 and B2) build trigonal planar B_4 units with a B–B distance of 1.78(5) Å in $(Ti_{1-x}V_x)_2Ir_2B_2$ and 1.85 Å in $TiMn_{0.92(2)}Ir_{2.08(2)}B_2$. The layer at z = 0 contains all other metals (Ti, Mn, Ti/V) and the third boron atom (B3). In this layer the M (Ti/V or Mn) atoms form equilateral triangles with a M–M distance of 2.72(2) Å (M = Ti/V) or 2.61(1) Å (M = Mn). Two M_3 triangles are stacked on top of each other, forming M_3 chains with an intrachain distance corresponding to the *c* lattice parameter at ca. 3.19 Å. The shortest distance between two Mn–atoms of two adjacent triangles in the same layer is 6.404(7) Å, which is more than twice as large as the distance in the *c* direction. These distances and the boron–metal and metal–metal distances are comparable to those found in $TiCrIr_2B_2$ and reported $Ti_{1+x}Os_{2-x}RuB_2$–type phases such as $Ti_{1.6}Os_{2.4}B_2$ and $Ti_{1-x}Fe_xOs_2RhB_2$ (0 < x < 0.5) [30]. All atoms at z = 0 are coordinated by prisms build by atoms in the z = 0.5 layers: trigonal prisms for boron and pentagonal prisms for Ti and M (Fig. 1a). Likewise, the boron atoms at z = 0.5 are coordinated by prisms of metals at z = 0, whereas the iridium atoms are coordinated by strongly distorted icosahedra of all atom. For clarity reasons, we will use the simplified formula $TiMIr_2B_2$ in the following discussion to represent these two phases.

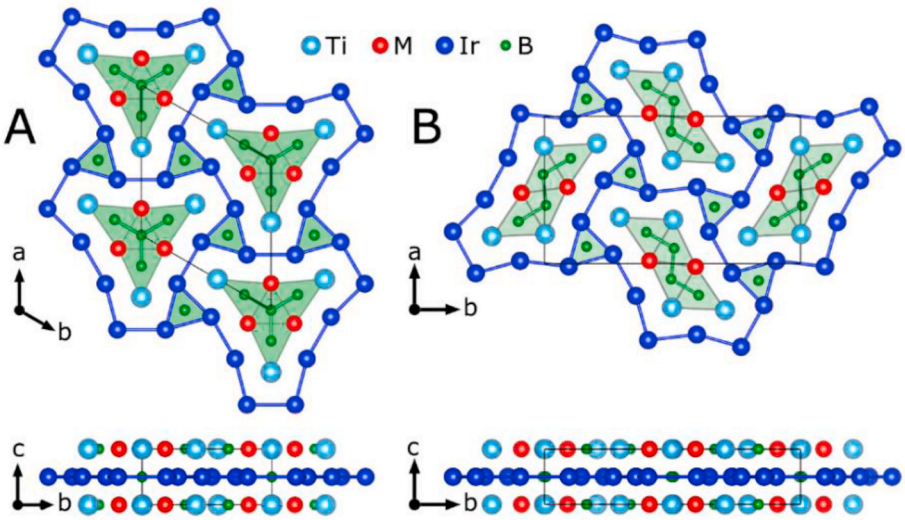

Fig. 1. Projections of the structures of **(a)** $TiMIr_2B_2$ (M = V, Mn; $Ti_{1+x}Os_{2-x}RuB_2$–type) and of **(b)** $Ti_2M_{1-x}Ir_{3+x}B_3$ (x < 0.2; M = Mn–Ni; $Ti_{1+x}Rh_{2-x+y}Ir_{3-y}B_3$–type) phases along [001] on top and along [100] at the bottom. The highlighted green triangles indicate boron–filled trigonal prisms. Note that for the M = V phase, the Ti and M positions are all filled by the mixed Ti/V atoms. (For interpretation of the references to colour in this figure legend, the reader is referred to the Web version of this article.)

The $TiMnIr_2B_2$-phase contains a magnetically active element (Mn), thus the Mn substructure (chains of Mn_3 triangles) has the potential to produce interesting magnetic properties. Unfortunately, only 6 wt.-% of this phase has been synthesized until now, so the magnetic properties cannot be studied at this time. Nevertheless, comparing this substructure with other will lead to a better understanding of the potential magnetic properties. For example, the similar Cr substructure has produced the isomorphic $TiCrIr_2B_2$ ferrimagnet. Another boride phase containing a similar substructure of a magnetic element is NbFeB (ZrNiAl–type structure) [31], also crystallizes in the hexagonal space group ($P\bar{6}2m$, no 189, Pearson symbol hP9) and contains trigonal boron–centered M_6B prisms. Thus, both structure types contain triangles of magnetic 3d transition metals. In contrast to the boron capped M_6B (M = Cr, Mn) prisms, the rectangular faces of the Fe_6B prisms in NbFeB are capped by Nb–atoms, resulting in isolated B atoms in the latter compound instead of trigonal B_4 fragments as found in $TiMIr_2B_2$. Nevertheless, the M_3 (M = Cr, Mn, Fe) triangles in these three compounds are very similar, having comparable intra-triangle distances of 2.64 Å (in Cr_3), 2.61 Å (in Mn_3) and 2.67 Å (in Fe_3) as well as similar inter-triangle distances of 3.18 Å (Fe_3 - Fe_3), 3.19 Å (Mn_3 - Mn_3) and 3.22 Å (Fe_3 - Fe_3). Consequently, the distances within the chains of M_3 triangles in these three compounds are nearly the same, but the distance between these chains is structure-type dependent: The interchain distance of 8.61 Å in $TiMnIr_2B_2$ is similar to that in $TiCrIr_2B_2$ (8.55 Å), whereas it is only 6.01 Å in NbFeB (both center–to–center), hinting at different magnetic properties for these two structure types despite the similar magnetic chains of M_3 triangles. Such studies of magnetic properties would be highly interesting both experimentally and theoretically, as they would help shed some light on the effects of different interchain distances.

$Ti_2M_{1-x}Ir_{3+x}B_3$ (x < 0.2; M = Mn–Ni): Analogous to the $Ti_{1+x}Os_{2-x}RuB_2$–type structure discussed above, the structure of $Ti_2M_{1-x}Ir_{3+x}B_3$ compounds ($Ti_{1+x}Rh_{2-x+y}Ir_{3-y}B_3$–type) displays two different layers at z = 0 and z = 0.5: Ti, M and isolated boron atoms are found at z = 0, while Ir and other B atoms (building zigzag B_4 fragments) fill the z = 0.5 layer.

Two M_2 dumbbells and two Ti atoms form a trigonal prism ($[Ti_2M_4]$B8 prism) which is centered by the inner B atom (B8) of the zigzag B_4 fragment. The outer B atoms (B7) of the zigzag B_4 fragment resides in the nearby trigonal prims which have the inverse Ti:M ratio ($[Ti_4M_2]$B7 prisms). The zigzag B_4 fragment arises from the rectangular face sharing of $[Ti_2M_4]$B8 and $[Ti_4M_2]$B7 prisms (Fig. 1b). The two other rectangular faces of these prisms are all capped by Ir atoms at $z = 0.5$. Six of those Ir atoms form another set of trigonal prims centered by the isolated B9 atoms ($[Ir_6]$B9 prism). Because the two layers at $z = 0$ and $z = 0.5$

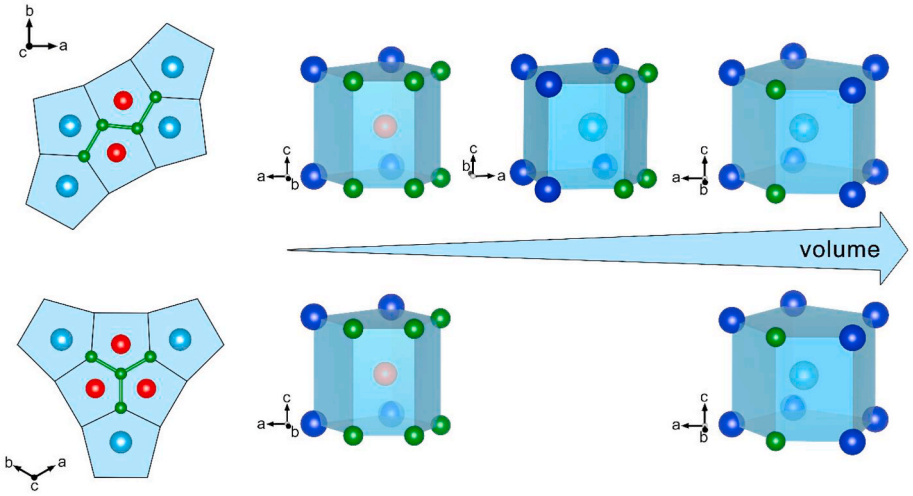

Fig. 2. Sets of pentagonal prisms centered by M (red) and Ti (cyan) in the orthorhombic $Ti_{1+x}Rh_{2-x+y}Ir_{3-y}B_3$–type structure (top) and the hexagonal $Ti_{1+x}Os_{2-x}RuB_2$–type structure (bottom). (For interpretation of the references to colour in this figure legend, the reader is referred to the Web version of this article.)

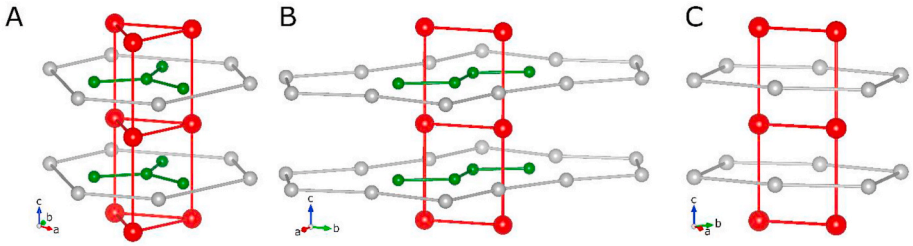

Fig. 3. Detailed view of the different M–substructures (M_3 chain and M_2 ladder) and coordination found in (a) the hexagonal $TiMIr_2B_2$ structure ($Ti_{1+x}Os_{2-x}RuB_2$–type), (b) in the orthorhombic $Ti_2MIr_3B_3$ structure ($Ti_{1+x}Rh_{2-x+y}Ir_{3-y}B_3$–type, right) and in the tetragonal $Ti_9M_2Ru_{18}B_8$ (M = Fe) structure.

alternate along the *c*–axis, all trigonal prims form infinite columns parallel to [001] by sharing their trigonal faces. Just as in the previous structure type, all atoms at z = 0 are coordinated by prisms build by atoms in the z = 0.5 layers including pentagonal prisms for Ti and M (Figs. 1 and 2). In contrast, only the boron atoms at z = 0.5 are coordinated by prisms of metals at z = 0, whereas the iridium atoms are coordinated by strongly distorted icosahedra of all atom types as previously described in $Ti_{1+x}Rh_{2-x+y}Ir_{3-y}B_3$ [22]. The B–B distance in this series varies from 1.81(4) Å for M = Ni to 1.90(4) Å for M = Mn. These phases are the first of this structure type containing a magnetic element (M), thus it is important to describe the substructure build by M: The shortest M–M distance, which is very similar in all phases and varies from 2.61(1) Å for M = Mn and Ni to 2.67(1) Å for M = Fe and Co, is consistent with M_2 dumbbells. The distance between dumbbells (inter–dumbbell distance) has the same length as the *c* lattice parameter (ca. 3.23 Å), thereby building a ladder substructure (M_2 chain). A similar ladder–like arrangement of magnetic Fe atoms (with Fe–Fe distances of 2.49 Å and 2.97 Å) has been observed in $Ti_9Fe_2Ru_{18}B_8$, and it is believed to have induced ferromagnetism in this phase [32]. However, the significant differences between these two types of ladder substructures (ca. 0.2 Å larger distances in the new substructure) can affect the magnetic properties. In particular, the proximity of the nearby B_4 fragments which strongly interact with the new ladders (Fig. 3b) in the new phases (absent in $Ti_9Fe_2Ru_{18}B_8$, Fig. 3c) may drastically impact the magnetic properties, as strong bonding between M and B will lower the electron density on M and thus reduce the strength of M–M magnetic interactions (a related manuscript on theoretical calculations will be communicated soon).

3.4. *Structural relationship between $Ti_{1-x}Rh_{2-x+y}Ir_{3-y}B_3$– and $Ti_{1-x}Os_{2-x}RuB_2$–type structures*

Using different *3d* transition metals for M (M = V - Ni) in the series $(Ti_{1-x}M_x)_3Ir_3B_3$ (x = 1/3, 1/2) results in the formation of hexagonal $Ti_{1-x}Os_{2-x}RuB_2$–type structure for M = V, Cr and Mn on the one hand and of orthorhombic $Ti_{1-x}Rh_{2-x+y}Ir_{3-y}B_3$–type structure for M = Mn, Fe, Co and Ni on the other hand. Moreover, in the case of M = Mn, both structures occur side by side. Comparing the two structure types, a close relationship between them becomes apparent: Both are layered along the c–axis, both have a metal–to–boron ratio M:B of 2:1 and both contain isolated boron as well as B_4 fragments. However, the B_4 unit is trigonal planar in the $Ti_{1-x}Os_{2-x}RuB_2$–type structure while it is zigzag shaped in the $Ti_{1-x}Rh_{2-x+y}Ir_{3-y}B_3$–type structure. Each boron atom of both B_4–units is located inside a trigonal prism made from M and Ti. The different topology of the B_4–fragment and ultimately the different space group symmetry of the structures depends only on how those trigonal prisms are connected. While three trigonal prisms in the $Ti_{1-x}Os_{2-x}RuB_2$-type structure are connected via one of their rectangular faces to a central trigonal prism, the trigonal prisms in the $Ti_{1-x}Rh_{2-x+y}Ir_{3-y}B_3$–type structure are all successively connected by their rectangular faces (Figs. 1 and 2).

The close relationship between the two structures raises the question why one is preferred over the other. By looking at the whole series one finds that for the larger *3d* transition metals (V, Cr, Mn) the hexagonal structure is preferred, while the smaller *3d* metals (Mn, Fe, Co, Ni) prefer the orthorhombic structure. Analyzing the coordination polyhedra (Fig. 2) around the metal atoms M and Ti, two different polyhedra exist

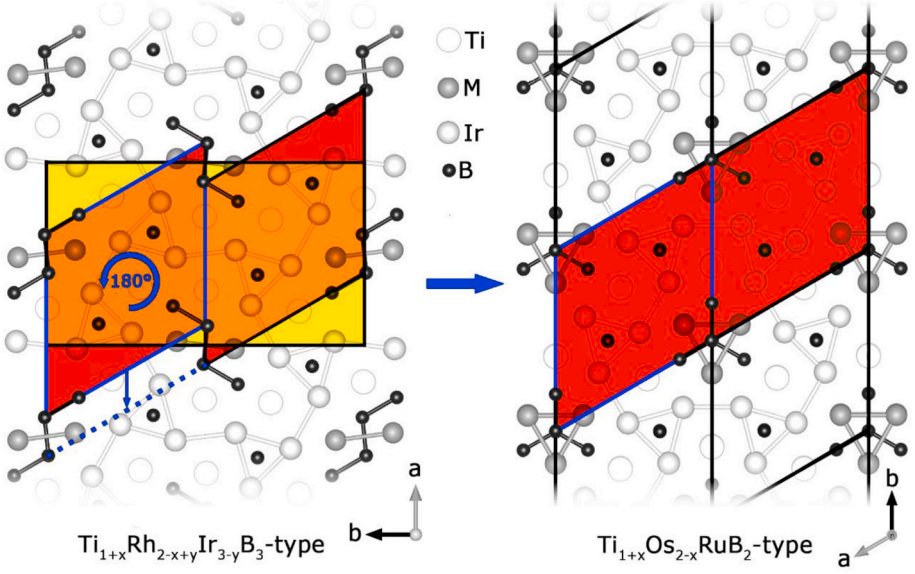

Fig. 4. Structural relation between the orthorhombic $Ti_{1+x}Rh_{2-x+y}Ir_{3-y}B_3$–type structure (left, unit cell shaded in yellow) and the hexagonal $Ti_{1+x}Os_{2-x}RuB_2$–type structure (right, unit cells shaded in red). (For interpretation of the references to colour in this figure legend, the reader is referred to the Web version of this article.)

for the hexagonal structure while three different polyhedra occur in the orthorhombic structure. Two out of three polyhedra of the orthorhombic structure are identical with the two polyhedra of the hexagonal structure. Accordingly, the orthorhombic structure contains a coordination polyhedron that does not exist in the hexagonal structure; thus, this explains the absence of a group-subgroup relationship between them.

The polyhedra have different volumes (Fig. 2), and the volume increases with decreasing number of boron atoms being part of the coordination polyhedron. The hexagonal structure contains the small polyhedron (six boron atoms participating) and the large polyhedron (two boron atoms involved). In the orthorhombic structure, however, an additional third coordination polyhedron exists and contains four boron atoms; thus, its volume lies in-between the previous two.

Naturally, we expect the large atoms to occupy the larger polyhedron, as it was found in the hexagonal structure of $TiCrIr_2B_2$, where Ti seats in the larger polyhedron while the smaller Cr atom occupies the smaller polyhedron. The same holds true for the hexagonal compounds with M = V and Mn.

Due to the presence of three different polyhedra, the situation is slightly more complex in the orthorhombic structures, but the general trend is the same. The Ti atoms occupy the large and the intermediate polyhedra, while the smaller M atoms (M = Mn, Fe, Co or Ni) are found inside the small polyhedron mixed with a small amount of Ir (the second largest metal atom, $r_{Ti} > r_{Ir} > r_M$).

The two different pentagonal prisms of the hexagonal structure occur three times each, while the three different pentagonal prisms of the orthorhombic structure occur twice each. Thus, the total number of pentagonal prisms is the same for both structures. Consequently, the ratio between the number of large sites (preferred by Ti) to the number of small sites (preferred by M) in the hexagonal structure is 1:1. In comparison, the ratio between the number of sites preferred by Ti to the number of sites preferred by M in the orthorhombic structure is 2:1, hinting at larger unit cells for the orthorhombic structure. Indeed, the average cell volume is 406.5 $Å^3$ for the hexagonal compounds and 415.8 $Å^3$ for the orthorhombic compounds.

As mentioned above, a group-subgroup relationship does not exist between the two structure types. Nevertheless, starting from the orthorhombic structure, one can derive the hexagonal structure with the following simple steps:

1) Identify two similar hexagonal unit cells (Fig. 4, left, red shadings) within the orthorhombic $Ti_{1+x}Rh_{2-x+y}Ir_{3-y}B_3$–type unit cell (Fig. 4, left, yellow shadings),
2) Rotate one hexagonal unit cell (Fig. 4, left, blue outline) by 180° around the *c*–axis, which produces the other adjacent hexagonal unit cell, and
3) Shift the rotated left hexagonal unit with respect to the other hexagonal cell along *a* by ca. 1.8 Å (blue arrow).
4) The hexagonal $Ti_{1+x}Os_{2-x}RuB_2$–type structure is obtained (Fig. 4, right).

No modification in *c* direction is required because of the same layered arrangement of both structures. This transformation can be considered as a form of glide-reflection twinning of the hexagonal structure [33].

4. Conclusion

We have synthesized and fully characterized new phases within the series $Ti_{2-x}M_{1+x-\delta}Ir_{3+\delta}B_3$ (x = 0.5 for M = V–Mn, x = 0 for M = Mn–Ni and $\delta < 0.2$), the main product is isostructural to hexagonal $Ti_{1+x}Os_{2-x}RuB_2$ for M = V–Mn, while for M = Fe, Co or Ni the $Ti_{1+x}Rh_{2-x+y}Ir_{3-y}B_3$–type structure is adopted, independent of the Ti:M ratio of the starting composition. For *M* = Mn, both structures were obtained side by side. The different Ti:*M* ratio (1:1 in the hexagonal and 2:1 in the orthorhombic) is attributed to differently sized polyhedra around these atoms, thereby directing the formation of each structure type. Moreover, the two structure types can be geometrically derived from each other, even though there is no obvious group–subgroup relationship.

Declaration of competing interest

The authors declare that they have no known competing financial interests or personal relationships that could have appeared to influence the work reported in this paper.

CRediT authorship contribution statement

Jan P. Scheifers: Investigation, Writing - original draft, Writing - review & editing. **Michael Küpers:** Methodology, Investigation. **Yuemei Zhang:** Supervision, Writing - review & editing. **Laura Lutz–Kappelman:** Visualization, Writing - review & editing. **Gordon J. Miller:** Supervision, Writing - review & editing. **Boniface P.T. Fokwa:** Conceptualization, Supervision, Writing - original draft, Writing - review & editing.

Acknowledgements

This work was supported by the National Science Foundation Career award to BPTF (no. DMR-1654780) as well as UC Riverside (Dissertation Year Award for JPS). We thank Dr. Christian Goerens (Umicore) for his contribution during the initial stages of this work.

Appendix A. Supplementary data

Supplementary data to this article can be found online at https://doi.org/10.1016/j.solidstatesciences.2020.106294.

References

[1] G. Akopov, M.T. Yeung, R.B. Kaner, Rediscovering the crystal chemistry of borides, Adv. Mater. 29 (21) (2017) 1604506, https://doi.org/10.1002/adma.201604506.
[2] T. Ma, H. Li, X. Zheng, et al., Ultrastrong boron frameworks in ZrB12: a highway for electron conducting, Adv. Mater. 29 (3) (2017) 1604003, https://doi.org/10.1002/adma.201604003.
[3] J.P. Scheifers, Y. Zhang, Fokwa BPT, Boron: enabling exciting metal-rich structures and magnetic properties, Acc. Chem. Res. 50 (9) (2017), https://doi.org/10.1021/acs.accounts.7b00268.
[4] M.T. Yeung, J. Lei, R. Mohammadi, et al., Superhard monoborides: hardness enhancement through alloying in $W_{1-x}Ta_xB$, Adv. Mater. 28 (32) (2016) 6993–6998, https://doi.org/10.1002/adma.201601187.
[5] I. Petsagkourakis, K. Tybrandt, X. Crispin, I. Ohkubo, N. Satoh, T. Mori, Thermoelectric materials and applications for energy harvesting power generation, Sci. Technol. Adv. Mater. 19 (1) (2018) 836–862, https://doi.org/10.1080/14686996.2018.1530938.
[6] J.V. Rau, A. Latini, New hard and superhard materials: $RhB_{1.1}$ and $IrB_{1.35}$, Chem. Mater. 21 (8) (2009) 1407–1409, https://doi.org/10.1021/cm900310j.
[7] B. Albert, H. Hillebrecht, Boron: elementary challenge for experimenters and theoreticians, Angew. Chem. Int. Ed. 48 (46) (2009) 8640–8668, https://doi.org/10.1002/anie.200903246.
[8] J.B. Levine, S.H. Tolbert, R.B. Kaner, Advancements in the search for superhard ultra-incompressible metal borides, Adv. Funct. Mater. 19 (22) (2009) 3519–3533, https://doi.org/10.1002/adfm.200901257.
[9] Q. Gu, G. Krauss, W. Steurer, Transition metal borides: superhard versus ultra-incompressible, Adv. Mater. 20 (19) (2008) 3620–3626, https://doi.org/10.1002/adma.200703025.
[10] H.Y. Chung, M.B. Weinberger, J.B. Levine, et al., Synthesis of ultra-incompressible superhard rhenium diboride at ambient pressure, Science 316 (5823) (2007) 436–439, https://doi.org/10.1126/science.1139322, 80-.
[11] M. Mbarki, R St Touzani, Fokwa BPT, Experimental and theoretical investigations of the ternary boride NbRuB with a layerlike structure type, Eur. J. Inorg. Chem. 2014 (8) (2014) 1381–1388, https://doi.org/10.1002/ejic.201301488.
[12] H. Jedlicka, F. Benesovsky, H. Nowotny, Die Kristallstruktur des W3CoB3 und der dazu isotypen Phasen Mo3CoB3, Mo3NiB3 und W3NiB3, Monatsh. Chem. 100 (3) (1969) 844–850, https://doi.org/10.1007/BF00900567.
[13] D. Kotzott, M. Ade, H. Hillebrecht, Synthesis and crystal structures of α- and β-modifications of Cr2IrB2 containing 4-membered B4 chain fragments, the τ-boride Cr7.9Ir14.1B6 and orthorhombic Cr2B, Solid State Sci. 10 (3) (2008) 291–302, https://doi.org/10.1016/j.solidstatesciences.2007.09.014.
[14] M. Ade, D. Kotzott, H. Hillebrecht, Synthesis and crystal structures of the new metal-rich ternary borides Ni12AlB8, Ni12GaB8 and Ni 10.6Ga0.4B6-examples for

the first B 5 zig-zag chain fragment, J. Solid State Chem. 183 (8) (2010) 1790–1797, https://doi.org/10.1016/j.jssc.2010.05.009.
[15] Fokwa BPT, M. Hermus, All-boron planar B6 ring in the solid-state phase Ti7Rh4Ir2B8, Angew. Chem. Int. Ed. 51 (7) (2012) 1702–1705, https://doi.org/10.1002/anie.201106798.
[16] W. Xie, H. Luo, K. Baroudi, J.W. Krizan, B.F. Phelan, R.J. Cava, Fragment-based design of NbRuB as a new metal-rich boride superconductor, Chem. Mater. 27 (4) (2015) 1149–1152, https://doi.org/10.1021/cm504449s.
[17] Q. Zheng, R. Gumeniuk, H. Rosner, et al., Synthesis, crystal structure and properties of the new superconductors TaRuB and NbOsB, J. Phys. Condens. Matter 27 (41) (2015) 415701, https://doi.org/10.1088/0953-8984/27/41/415701.
[18] M. Küpers, L. Lutz-Kappelman, Y. Zhang, G.J. Miller, Fokwa BPT, Spin frustration and magnetic ordering from one-dimensional stacking of Cr_3 triangles in $TiCrIr_2B_2$, Inorg. Chem. 55 (11) (2016) 5640–5648, https://doi.org/10.1021/acs.inorgchem.6b00714.
[19] M. Mbarki, R. StTouzani, Fokwa BPT, Unexpected synergy between magnetic iron chains and stacked B_6 rings in $Nb_6Fe_{1-x}Ir_{6+x}B_8$, Angew. Chem. Int. Ed. 53 (48) (2014) 13174–13177, https://doi.org/10.1002/anie.201406397.
[20] N. Sharma, M. Mbarki, Y. Zhang, A. Huq, Fokwa BPT, Structural-distortion-driven magnetic transformation from ferro- to ferrimagnetic iron chains in B_6 -based $Nb_6FeIr_6B_8$, Angew. Chem. Int. Ed. 57 (32) (2018) 10323–10327, https://doi.org/10.1002/anie.201804841.
[21] P. Rogl, F. Benesovsky, H. Nowotny, Über einige Komplexboride mit Platinmetallen, Monatsh. Chem. 103 (4) (1972) 965–989, https://doi.org/10.1007/BF00905170.
[22] C. Goerens, Fokwa BPT, The complex metal-rich boride Ti 1xRh 2-xyIr 3-yB 3 (x=0.68, y=1.06) with a new structure type containing B 4 zigzag fragments: synthesis, crystal chemistry and theoretical calculations, J. Solid State Chem. 192 (2012) 113–119, https://doi.org/10.1016/j.jssc.2012.04.005.
[23] Fokwa BPT, J. Von Appen, R. Dronskowski, Synthesis of a missing structural link: the first trigonal planar B 4 units in the novel complex boride Ti1+xOs 2-xRuB2 (x = 0.6), Chem. Commun. (42) (2006) 4419–4421, https://doi.org/10.1039/b608903h.
[24] J. Rodríguez-Carvajal, Recent advances in magnetic structure determination by neutron powder diffraction, Phys. B Condens. Matter 192 (1-2) (1993) 55–69, https://doi.org/10.1016/0921-4526(93)90108-I.
[25] J. Rodriguez-Carvajal, FullProf: a program for rietveld refinement and profile matching analysis of complex powder diffraction patterns, in: Satellite Meeting on Powder Diffraction of the XV Congress of the IUCr, 1990, p. 127. Toulouse.
[26] G.M. Sheldrick, A short history of SHELX, Acta Crystallogr Sect A Found Crystallogr 64 (1) (2008) 112–122, https://doi.org/10.1107/S0108767307043930.
[27] G.M. Sheldrick, Crystal structure refinement with SHELXL, Acta Crystallogr Sect C Struct Chem 71 (2015) 3–8, https://doi.org/10.1107/S2053229614024218.
[28] V.N. Eremenko, T.D. Shtepa, V.G. Sirotenko, Intermediate phases in alloys of titanium with iridium, rhodium, and osmium, Sov. Powder Metall. Met. Ceram. 5 (6) (1966) 487–490, https://doi.org/10.1007/BF00775541.
[29] O. Sologub, P. Rogl, G. Giester, The tau-borides τ-(Fe0.54Ir0.46)20Fe3B6 and τ-(Co0.64Ir0.36)21Co0.16B4B6, Intermetallics 18 (4) (2010) 694–701, https://doi.org/10.1016/j.intermet.2009.11.010.
[30] Fokwa BPT, R. Dronskowski, New transition-metal borides containing trigonal-planar B 4 -units: syntheses and single-crystal structure analyses of Ti 1.6 Os 2.4 B 2 and Ti 1-x Fe x Os 2 RhB 2, Z. Anorg. Allg. Chem. 634 (11) (2008) 1955–1960, https://doi.org/10.1002/zaac.200800219.
[31] Y. Kuzma, T. Tsolkovskii, O. Baburova, The systems Nb-Fe-B and Nb-Co-B, Inorg. Mater. 4 (7) (1968) 950–953.
[32] Fokwa BPT, G.D. Samolyuk, G.J. Miller, R. Dronskowski, Ladders of a magnetically active element in the structure of the novel complex boride $Ti_9Fe_2Ru_{18}B_8$: synthesis, structure, bonding, and magnetism, Inorg. Chem. 47 (6) (2008) 2113–2120, https://doi.org/10.1021/ic7020963.
[33] B.G. Hyde, S. Andersson, M. Bakker, C.M. Plug, M. O'Keeffe, The (twin) composition plane as an extended defect and structure-building entity in crystals, Prog. Solid State Chem. (1979), https://doi.org/10.1016/0079-6786(79)90002-5.